



RESEARCH ARTICLE

10.1029/2018JB015918

Seismic Dispersion and Attenuation in Saturated Porous Rock With Aligned Slit Cracks

Bo-Ye Fu<sup>1,2,3,4</sup>, Junxin Guo<sup>3,5</sup>, Li-Yun Fu<sup>1,5</sup>, Stanislav Glubokovskikh<sup>3</sup>, Robert J. Galvin<sup>3</sup>, and Boris Gurevich<sup>3,6</sup>

Key Points:

- We have quantified attenuation and dispersion due to presence of slit (2-D) cracks in a saturated porous rock
- The results show similarity of the dispersion and attenuation to effect caused by penny-shaped cracks but with difference at low frequencies
- In addition to the complete numerical solution of the problem, we have proposed an analytical approximation for the entire frequency range

<sup>1</sup>Key Laboratory of Earth and Planetary Physics, Institute of Geology and Geophysics, Chinese Academy of Sciences, Beijing, China, <sup>2</sup>Institutions of Earth Science, Chinese Academy of Sciences, Beijing, China, <sup>3</sup>Department of Exploration Geophysics, Curtin University, Perth, Western Australia, Australia, <sup>4</sup>College of Earth and Planetary Sciences, University of Chinese Academy of Sciences, Beijing, China, <sup>5</sup>School of Geosciences, China University of Petroleum (East China), Qingdao, China, <sup>6</sup>CSIRO, Kensington, Western Australia, Australia

Correspondence to:

J. Guo and L.-Y. Fu, junxin.guo@postgrad.curtin.edu.au; lfu@mail.iggcas.ac.cn

Citation:

Fu, B.-Y., Guo, J., Fu, L.-Y., Glubokovskikh, S., Galvin, R. J., & Gurevich, B. (2018). Seismic dispersion and attenuation in saturated porous rock with aligned slit cracks. *Journal of Geophysical Research: Solid Earth*, 123, 6890–6910. <https://doi.org/10.1029/2018JB015918>

Received 6 APR 2018

Accepted 6 AUG 2018

Accepted article online 14 AUG 2018

Published online 29 AUG 2018

Abstract

We estimate the seismic attenuation and velocity dispersion induced by fluid pressure diffusion in a saturated porous medium containing a sparse distribution of aligned slit fractures. This is done by solving the scattering problem for a single crack and using Waterman-Truell scattering approximation for a distribution of cracks. This approach gives a numerical solution for the entire frequency range and analytical solutions for the low- and high-frequency limits. Analysis of the results shows that the characteristics of the seismic dispersion and attenuation for the slit cracks are similar to known results for penny-shaped crack. At high frequencies, the attenuation and dispersion are controlled by the crack density regardless of the crack geometry. At low frequencies, due to the different geometries of the slit and penny-shaped cracks, the characteristics of seismic dispersion and attenuation are different. For both the slit and penny-shaped crack case, the slope of the frequency dependence attenuation of factor (inverse quality factor)  $Q^{-1}$  tends to be 1. Yet the low-frequency asymptotic solutions for these two cases are somewhat different. For penny-shaped cracks, the  $Q^{-1}(\omega)$  on the bilogarithmic scale has a straight line asymptote with slope 1, so that the attenuation factor at low frequencies is proportional to the frequency  $\omega$ . However, for slit cracks, the asymptotic low-frequency solution contains a logarithmic function of  $\omega$ , and no such asymptote exists. At the same time, similarly to the penny-shaped crack case, the solution for compressional velocity in the low-frequency limit is consistent with the anisotropic Gassmann theory.

1. Introduction

Understanding the role of fractures in rocks is important for studying earthquake mechanisms, safe drilling, and efficient reservoir exploitation (e.g., Guo et al., 2009; Kawahara, 1992; Kawahara & Yamashita, 1992). Techniques aimed to detect and characterize fracture networks have attracted substantial attention (e.g., Guo & Fu, 2007; Maultzsch et al., 2003; Peacock et al., 1994). Liu et al. (2007) analyzed the difference between the relative information contained in static and dynamic seismic attributes in both dry and saturated fractured rocks. In particular, for saturated porous rock, seismic attenuation is recognized as a potentially important parameter for characterizing fracture networks (Ba et al., 2011; Guo, Rubino, Glubokovskikh, et al., 2018; Hu et al., 2017; Liu et al., 2007; Wei & Fu, 2014).

An important mechanism for the seismic attenuation is the wave-induced fluid flow (WIFF) between the fractures and the porous background medium (e.g., Chapman, 2003; Galvin & Gurevich, 2006, 2007, 2009; Jakobsen et al., 2003; Quintal et al., 2014; Tisato & Quintal, 2013). A number of theoretical models have been proposed to study the seismic dispersion and attenuation due to WIFF between fractures and the background medium. One method is to treat the fractures and the pores as perturbations to the elastic background medium. Using this method, Hudson et al. (1996) modeled the WIFF effects induced by a single penny-shaped crack. This concept was further developed by Chapman (2003), Jakobsen et al. (2003), Jakobsen (2004), and Chapman et al. (2006), who studied the seismic dispersion and attenuation in saturated rocks with randomly distributed penny-shaped cracks and systems of larger aligned fractures.

An alternative method to model the WIFF effect is to consider fractures as inclusions or discontinuities in a porous background medium, which is described by Biot's poroelastic equations. Using this method, Galvin and Gurevich (2006, 2007, 2009) analyzed seismic dispersion and attenuation (far field properties) in a medium with aligned sparsely distributed penny-shaped cracks. Furthermore, Phurkhao (2013a, 2013b)

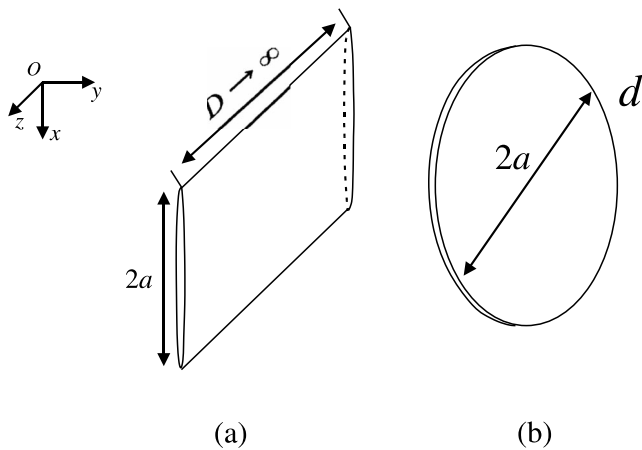


**Figure 1.** Three-dimensional sketch of slit and penny-shaped fractures, (a) slit fracture, and (b) penny-shaped fracture.

and Song et al. (2017a, 2017b) studied near-field properties of the scattered field for both penny-shaped and slit cracks, based on the poroelastic equations. An advantage of this approach is that fractures often cause a smaller effect on elastic properties than pores and hence can be treated using a first-order perturbation of the poroelastic medium.

Most of the research discussed above considers the fractures to be circular oblate spheroids or discs (sometimes these fractures are called penny-shaped). However, in reality, many fractures can have a shape more similar to that of slit fractures (3-D sketches of slit and penny-shaped fractures are shown in Figure 1). For instance, in carbonate, tight sand, or shale reservoirs, fracture “swarms” or “corridors” usually play an important role for fluid flow and wave scattering as the size of these fractures in such fractured zones is often comparable or even larger than the seismic wavelength (e.g., Vlastos et al., 2003, 2006, 2007; Guo, Rubino, Barbosa, et al., 2018a). In these fractured zones, there are usually densely spaced fractures tens of meters in height, several hundred meters in length, up to several meters in width, and with permeability on the order of several

Darcies (Bush, 2010). The length of these fractures is much larger than the other two dimensions, which makes them more similar in shape to slit fractures, rather than penny-shaped fractures. Hence, it is important to develop a theoretical model to describe the seismic dispersion and attenuation due to WIFF in saturated porous rock with slit fractures.

In addition to theoretical studies, the WIFF effect in fractured saturated rock has been studied numerically. Numerical simulations can handle more complex fracture systems than analytical models. Masson and Pride (2007) and Ba et al. (2008) modeled the mesoscopic fluid flow using finite difference method and pseudo spectral method, respectively. Rubino et al. (2009, 2014, 2015, 2016) have explored the frequency-dependent elastic properties of porous rocks induced by the WIFF effect using finite element method applied to Biot’s poroelastic equation (Biot, 1941, 1962). To reduce the computational cost and improve the simulation efficiency, the numerical simulations are usually performed in two dimensions, which implies that the fractures are slit shaped. Guo et al. (2017), Guo, Rubino, Barbosa, et al., (2018a), Guo, Rubino, Barbosa, et al., (2018b), and Guo, Rubino, Glubokovskikh, et al., (2018) compared the results of numerical simulations for slit fractures (2-D numerical simulation) against the theoretical model designed for the penny-shaped fractures (Galvin & Gurevich, 2009; a 3-D theoretical result) and found a surprisingly good agreement, despite the difference in underlying geometries. This phenomenon was further explored in recent numerical simulations of Hunziker et al. (2018), which show that attenuation and dispersion caused by 3-D cracks is very close to that caused by 2-D cracks. Although there is no clear theoretical explanation as yet for this agreement, it implies that the seismic dispersion and attenuation due to WIFF is relatively insensitive to the largest dimension (“length”) of the fractures. Direct validation of the similarity and difference between the scattering properties of penny-shaped and slit cracks requires an explicit comparison of theoretical models for penny-shaped (3-D) and slit (2-D) fractures. However, to the authors’ knowledge, no theoretical model for the slit fractures currently exists.

In this paper, three objectives are set. Our first aim is to estimate the dispersion and attenuation of seismic waves that takes place in a porous medium containing a sparse distribution of aligned slit fractures (Figure 2). This is done by combining the theory of poroelasticity (Biot, 1962) with the multiple-scattering theory of Waterman and Truell (1961). Next, we deduce the asymptotic solutions at low and high frequencies and then compare them with corresponding asymptotes developed for penny-shaped fractures. Finally, we attempt to construct a closed form approximate solution for the entire frequency range. Note that the “entire frequency range” is meant here with respect to fluid pressure diffusion, and the low and high frequencies we evaluate here are with respect to

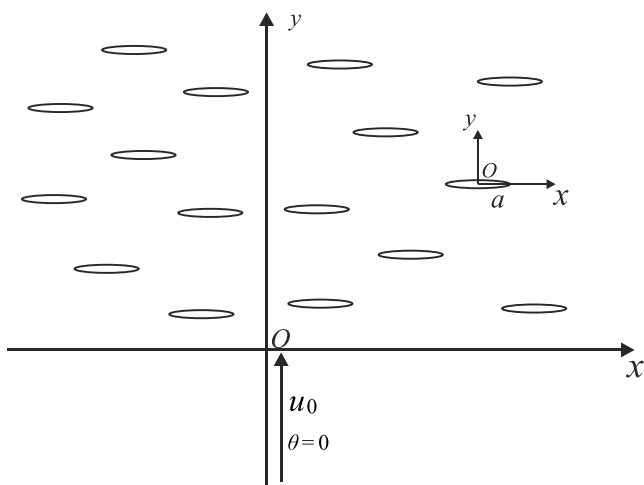


**Figure 2.** Infinite elastic background medium embedded with randomly and sparsely distributed aligned slit fractures; the length and thickness of the fracture is  $2a$  and infinitesimal, respectively.

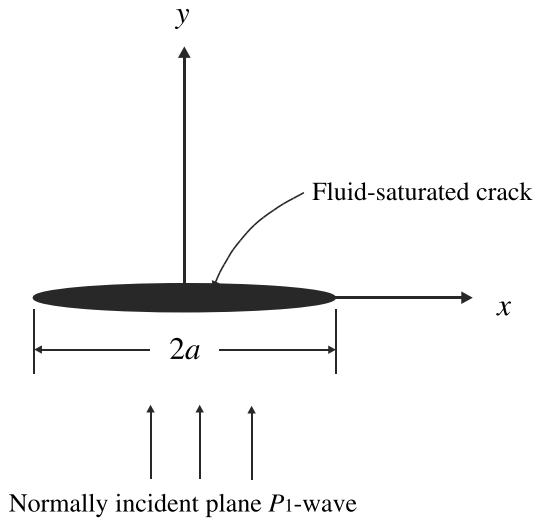


**Figure 3.** Fluid-saturated slit crack in a poroelastic solid.

the extent to which fluid is able to diffuse between cracks and pores during the propagation of the seismic wave. The wave propagation is still considered in the low-frequency regime of Biot theory (Biot, 1956a) where viscous forces dominate over inertial ones, and the cracks are assumed to be much smaller than the seismic wavelength, so that the scattering effects are negligible.

## 2. Theoretical Derivation

### 2.1. Scattering by a Single Crack

To estimate the attenuation and dispersion of elastic waves taking place in a porous medium containing a sparse distribution of aligned slit cracks, the scattering properties of a single slit crack are required. We first consider the scattering properties of a plane wave by a single slit crack which is infinite along the  $z$ -direction but has finite length  $2a$  in the  $x$  direction and infinitesimal thickness in the  $y$  direction. In such a medium, propagation of waves in the  $x$ - $y$  plane poses a 2-D problem, as shown in Figure 3 (origin is located at the center of the crack). A plane compressional wave propagates normally to the crack surfaces. We

assume that fractures are embedded in a porous elastic solid saturated by a single-phase viscous fluid and are hydraulically connected to the adjacent pores. In a porous medium, the solid and relative fluid displacements in response to stress are described by Biot's dynamic poroelastic equations (Biot, 1962).

Derivation of the scattered field requires the knowledge of the boundary conditions on the crack surfaces, which are the same as for a circular crack (Galvin & Gurevich, 2007; Song et al., 2017a). Due to the infinitesimal thickness of the crack, the scattered displacement vectors should be symmetric about the  $x$  axis (Figure 3). Thus, the scattered shear stress and the scattered normal component of the solid and fluid displacements must be zero outside the crack. As mentioned earlier, the cracks are assumed to be in hydraulic communication with the surrounding porous medium. For a fluid-filled permeable crack, there are no shear tractions acting on the surface, and the continuity of the normal traction requires that the normal stress is equal to the negative of the fluid pressure in the crack. The incident wave is a plane  $P$  wave. Based on the Biot's poroelastic equations and boundary conditions, we can obtain a unique solution of the scattered field by a single crack. The details of the solution are shown in Appendix A.

### 2.2. A Sparse Distribution of Cracks

Dispersion and attenuation of a seismic wave propagating in a medium with a random distribution of aligned cracks can be estimated using the multiple-scattering theorem of Waterman and Truell (1961), based on the far-field amplitude scattered by a single crack (Appendix A). According to Waterman and Truell (1961), the effective wave number  $k^*$  for the medium with cracks in terms of the number of scatterers per unit volume  $n_0$  and the forward far-field scattering amplitude  $f(0)$  for a single scatterer can be expressed as

$$k^* = k_1 \left[ 1 + \frac{4\pi n_0 f(0)}{k_1^2} \right]^{\frac{1}{2}} \approx k_1 \left[ 1 + \frac{2\pi n_0 f(0)}{k_1^2} \right], \quad (1)$$

where  $f(0)$  is the forward scattering amplitude which can be expressed as (see Appendix B)

$$f(0) = -j \frac{A_1(0) k_1^2}{\pi}. \quad (2)$$

In this expression (see Appendix A)

$$A_1(k) = \frac{\pi(\chi_3 - \chi_2)(k^2 - \sigma_3 k_1^2) B(k)}{E \eta_1}, \quad (3)$$

which is the displacement potential amplitude in wave number domain in  $x$  direction scattered by a single crack (see Appendix A and Song et al., 2017b).  $k$  is the radial wave number of scattered wave, and  $\eta_i = \sqrt{k^2 - k_i^2}$  is the axial wave number.

To obtain  $A_1(0)$  we have to put  $k = 0$  in equation (3). Then, substituting equation (3) into (2) gives

$$f(0) = \frac{(H - \alpha M) H k_1}{2\mu^2 k_3^2 (\mu - H + \alpha M)} B(0), \quad (4)$$

where  $\mu$  is the shear modulus of the solid frame and  $\alpha = 1 - K_d/K_g$  is the Biot-Willis coefficient (Biot & Willis, 1957). The coefficient  $K_d$  is the bulk modulus of the dry rock frame,  $K_g$  is the bulk modulus of the solid grain material,  $M$  is the pore so-called space modulus,  $H$  is undrained  $P$  wave modulus of the saturated poroelastic medium, and  $\chi_i$  ( $i = 1, 2, 3$ ) and  $\sigma_j$  ( $j = 1, 2, 3, 4$ ) are intermediate variables given in Appendix A.  $B(k)$  is the solution of a Fredholm integral equation in Appendix A (equation (A23)).  $k_1$ ,  $k_2$ , and  $k_3$  are the wave numbers of  $P_1$  (fast compressional),  $P_2$  (slow compressional), and  $S$  (shear) waves, respectively, which can be expressed as

$$k_1 = \sqrt{\frac{\rho\omega^2}{H}}, \quad (5)$$

$$k_2 = \sqrt{\frac{ibH\omega}{LM}}, \quad (6)$$

$$k_3 = \sqrt{\frac{\rho\omega^2}{\mu}}, \quad (7)$$

where  $b = \eta/\kappa$ .  $L = K_d + 4/3 \mu$  is the  $P$  wave modulus of the solid rock frame.  $\rho$  is the density of the overall fluid-saturated medium.  $\kappa$  is the rock permeability,  $\eta$  is the shear viscosity of the pore fluid, and  $\omega$  is the angular frequency.

The real part of the wave number  $k^*$  given by equation (1) gives the effective velocity  $v^*$  in the medium with a low concentration of scatterers,

$$v^* = \frac{v_1}{\left[1 + \frac{2\pi n_0}{k_1^2} \operatorname{Re}\{f(0)\}\right]}, \quad (8)$$

where  $v_1 = \omega/k_1 = \sqrt{H/\rho}$  is the velocity of the fast compressional ( $P_1$ ) wave in the crack-free fluid-saturated porous medium. The imaginary part of  $k^*$  gives the dimensionless attenuation (inverse quality factor)

$$Q^{-1} = \frac{4\pi n_0}{k_1^2} \operatorname{Im}\{f(0)\}. \quad (9)$$

Equations (8), (9), and (4) show that estimation of the  $P$  wave dispersion and attenuation requires the knowledge of  $B(0)$  only. As shown in Appendix A,  $B$  is a solution of an integral equation (A23), which does not have a general analytical solution for the entire frequency range, and needs to be solved for every frequency numerically. However, in the limiting cases of low and high frequencies,  $B$  has closed-form asymptotic analytical expressions. Numerical and asymptotic analytical solutions will be presented in sections 3 and 4. We present numerical results first to see the behavior of the general solution and help guide the derivation of the asymptotic solutions.

### 3. Numerical Results

The numerical solution for  $B$  can be obtained by the method of quadratures (see e.g., Galvin & Gurevich, 2007; Kawahara & Yamashita, 1992). We illustrate this by an example of a porous material considered by Rubino et al. (2015) and Guo, Rubino, Barbosa, et al. (2018a): Grain bulk modulus is  $K_g = 37$  GPa, dry bulk modulus  $K_d = 26$  GPa, shear modulus  $\mu = 31$  GPa, porosity  $\phi = 10\%$ , and permeability  $\kappa = 10^{-4}$  mD ( $10^{-19}$  m<sup>2</sup>). The fractures and the embedding background are fully saturated with water, with bulk modulus  $K_f = 2.25$  GPa and viscosity  $\eta = 0.001$  Pa · s. The length of the slit fractures is 4 cm. The number of scatterers per unit volume  $n_0$  is 0.01. Using these parameters, we can solve equation (A23) numerically using the workflow described in Appendix A.

Figures 4a and 4b show the numerical solutions for effective velocity (equation (8) normalized by crack-free saturated velocity  $v_1$ ) and dimensionless attenuation (equation (9)) as functions of dimensionless frequency  $|k_2 a|^2$ . Also shown in Figures 4a and 4b are asymptotic solutions at low and high frequencies as well as

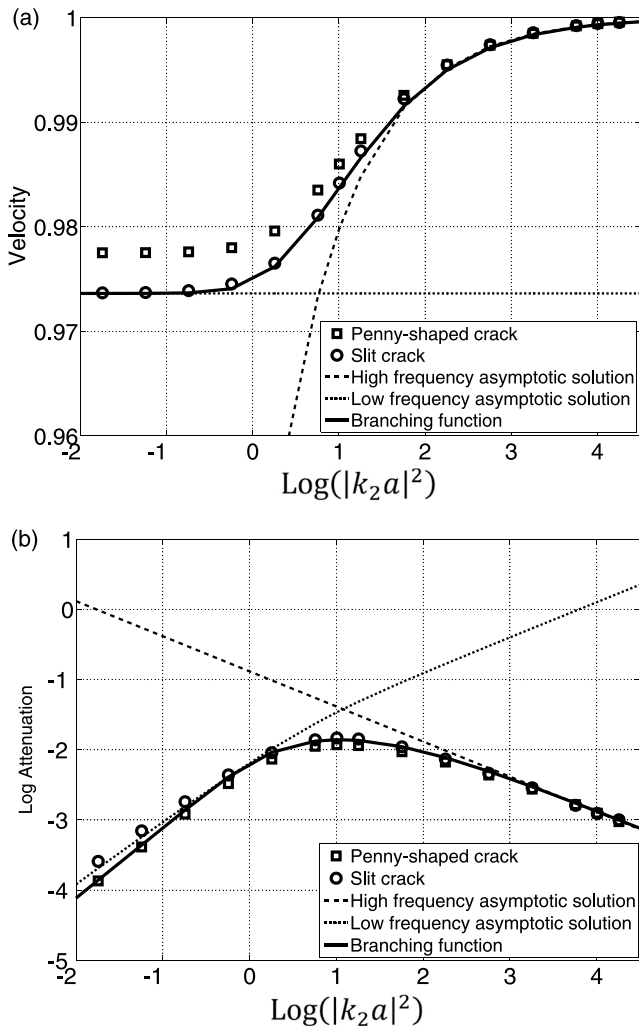


**Figure 4.** (a) Dimensionless velocity and (b)  $\log(1/Q)$  as a function of a dimensionless frequency parameter  $\log(|k_2a|^2)$ ; the black circles and black rectangles represent numerical results for slit cracks and penny-shaped cracks, respectively; the dotted and dashed lines are the low- and high-frequency asymptotes, respectively; the solid line is the branching function approximation.

the branching function approximation discussed in sections 4 and 5. For comparison, we also show the numerical results for the penny-shaped crack case, calculated by the computer program of Galvin (2007).

The numerical results for slit and penny-shaped cracks are similar. At high frequencies, the velocities and attenuation factors are consistent with each other. At low frequencies, the results are similar, but not the same. For the slit crack, the decrease of the velocity is about 2.5%, while for the penny-shaped crack, it is about 2%. The attenuation for slit crack is also higher than for the penny-shaped crack in the low-frequency region. The maximum attenuation value is 0.0147 for slit crack, and it is 0.0118 for penny-shaped crack, for which the attenuation is about 25% higher than that for the penny-shaped crack case. The similarities and differences between the slit and penny-shaped crack cases will be further discussed in section 4.

#### 4. Analytical Solution

The numerical results obtained in section 3 give the velocity dispersion and attenuation in the entire frequency range, which is general regardless of the size of the crack with respect to the incident wavelength. The velocity and attenuation are obtained through numerical methods. While the numerical method described above gives the complete solution for the velocity and attenuation as functions of frequency, for the analysis of the properties of the solution and sensitivity to various parameters, it is useful to derive some asymptotic approximations. Here we derive such approximations in the limits of low and high frequencies. Note that the low and high frequencies we evaluate here are with respect to the extent to which fluid is able to diffuse between crack and pore space during the propagation of the seismic wave, and we are still in the low-frequency regime of Biot theory, which means the radial wave number satisfies the condition  $k \gg k_3 > k_1$ . At low frequencies, due to the large fluid-diffusion length, velocity dispersion and attenuation should be affected by the fracture distribution, and the diffusion length can be taken large compared with the crack radius, or  $|k_2a| \ll 1$ . At high frequencies, the fluid flow between background pores and fractures is negligible, and therefore, the diffusion length can be taken as small compared with the crack radius, which means  $|k_2a| \gg 1$ . The detail of derivation of the analytical solutions is given in Appendix C. Here we present an analysis of these solutions.

##### 4.1. Low-Frequency Asymptote

As shown in section 2, velocity and attenuation can be obtained, if the value of  $f(0)$  is known. In the low-frequency limit, the value  $f_{\text{low}}(0)$  is given by (see Appendix C)

$$f_{\text{low}}(0) = \frac{(H - \alpha M)^2}{8\mu(H - \mu - \alpha M)} a^2 + \frac{\alpha M(H - \alpha M)^2}{8\mu(\mu - H + \alpha M)^2} \left[ \left( \frac{L}{\alpha\mu} \right) k_2^2 a^2 \int_0^\infty \frac{J_1^2(x)}{x^2 \sqrt{x^2 - (k_2 a)^2}} dx - \frac{1}{2} i \text{Im} \left( \int_0^\infty \frac{J_1^2(x)}{\sqrt{x^2 - (k_2 a)^2}} dx \right) \right], \quad (10)$$

where  $J_1(x)$  is the first-order Bessel function.

By substituting equation (10) into (8) and taking the real part, the expression for effective velocity at low frequencies can be obtained

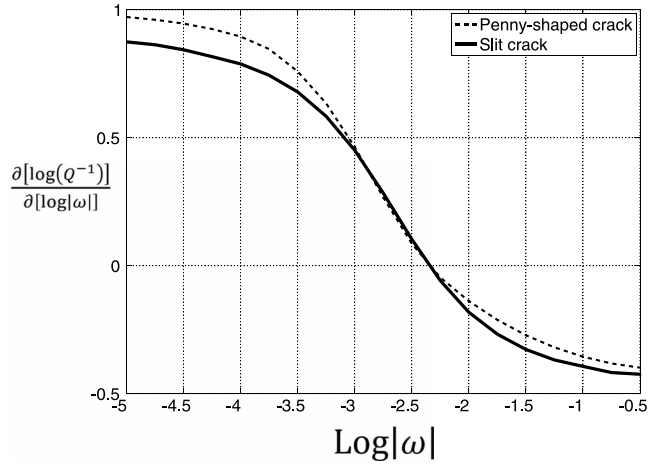


**Figure 5.** The variation of  $\partial[\log_{10}Q_{\text{low}}^{-1}]/\partial[\log(\omega)]$  versus  $\log(\omega)$  for the entire frequency region.

$$v_{\text{low}}^* = \frac{v_1}{\left[1 + \frac{2\pi n_0}{k_1^2} \text{Re}\{f_{\text{low}}(0)\}\right]} = \frac{v_1}{\left[1 + \frac{\pi(H - \alpha M)^2 \varepsilon}{4\mu(H - \mu - \alpha M)}\right]} = v_1 \left[1 - \frac{\pi(H - \alpha M)^2 \varepsilon}{4\mu(H - \mu - \alpha M)}\right] \quad (11)$$

which is shown as the black dotted line in Figure 4a.

The low-frequency attenuation  $Q^{-1}$  is defined by the imaginary part of the function  $f_{\text{low}}(0)$ ,

$$Q_{\text{low}}^{-1} = \frac{4\pi n_0}{k_1^2} \text{Im}\{f_{\text{low}}(0)\} = \frac{\alpha M(H - \alpha M)^2 \pi \varepsilon}{2(\mu - H + \alpha M)^2 \mu} \left[ \frac{L}{\alpha \mu} |k_2 a|^2 \left( \int_0^\infty \frac{J_1^2(x)}{x^2 \sqrt{x^2 - (k_2 a)^2}} dx \right) - \frac{1}{2} \text{Im} \left( \int_0^\infty \frac{J_1^2(x)}{\sqrt{x^2 - (k_2 a)^2}} dx \right) \right] \quad (12)$$

shown as the black dotted line in Figure 4b. The terms  $\left(\int_0^\infty \frac{J_1^2(x)}{x^2 \sqrt{x^2 - (k_2 a)^2}} dx\right)$  and  $\frac{1}{2} \text{Im} \left(\int_0^\infty \frac{J_1^2(x)}{\sqrt{x^2 - (k_2 a)^2}} dx\right)$  are related to  $|k_2 a|$ . When  $|k_2 a| \rightarrow 0$ , they can be approximated as

$$\int_0^\infty \frac{J_1^2(x)}{x^2 \sqrt{x^2 - (k_2 a)^2}} dx \approx -\frac{1}{8} \ln(|k_2 a|^2) + c_1, \quad (13)$$

and

$$\frac{1}{2} \text{Im} \left( \int_0^\infty \frac{J_1^2(x)}{\sqrt{x^2 - (k_2 a)^2}} dx \right) \approx |k_2 a|^2 \left[ -\frac{1}{32} \ln(|k_2 a|^2) + c_2 \right], \quad (14)$$

where  $c_1$  and  $c_2$  are constants, given as  $c_1 \approx 0.2677$  and  $c_2 \approx 0.0349$ . Substituting equations (13) and (14) into (12) gives

$$Q_{\text{low}}^{-1} = \pi \varepsilon \frac{M(H - \alpha M)^2}{2\mu^2(\mu - H + \alpha M)^2} |k_2 a|^2 \left[ \frac{1}{32} (\alpha \mu - 4L) \ln(|k_2 a|^2) + (Lc_1 - \alpha \mu c_2) \right]. \quad (15)$$

In equations (11) (12), and (15),  $\varepsilon$  is the crack density parameter (Hudson, 1980), defined as  $\varepsilon = n_0 a^2$  for slit cracks (Kachanov, 1992; Kachanov & Sevostianov, 2005). Because of the existence of the term  $\ln(|k_2 a|^2)$ , the low-frequency behavior of attenuation for the slit cracks is different from the behavior for the penny-shaped cracks. For penny-shaped cracks, the low-frequency  $Q^{-1}$  is proportional to dimensionless frequency  $|k_2 a|^2$  (Galvin & Gurevich, 2009), which is a straight line with slope  $\partial[\log(Q^{-1})]/\partial \log(\omega) = 1$  on bilogarithmic scale. In contrast, for the slit cracks, at low frequencies, we have a logarithmic relationship (15) between  $Q^{-1}$  and  $|k_2 a|^2$ ; on bilogarithmic scale this is a curve whose slope  $\partial[\log(Q^{-1})]/\partial \log(\omega)$  is decreasing with decreasing frequencies.

Figure 5 shows the slope  $\partial[\log(Q^{-1})]/\partial[\log(\omega)]$  versus  $\log(\omega)$  for both penny-shaped and slit crack cases. This plot shows that with the decrease of the frequency, this slope for both penny-shaped and slit crack cases approaches 1. However, for slit cracks, the slope approaches the asymptotic value of 1 much slower than for penny-shaped cracks. To illustrate this result analytically, we derive the asymptotic behavior of slope  $\partial[\log(Q^{-1})]/\partial[\log(\omega)]$  in low-frequency region.

At low frequencies, attenuation for penny-shaped cracks is given by (Galvin & Gurevich, 2009)

$$Q_{\text{low-3D}}^{-1} = \frac{2M(H - \alpha M)^2(2 - 4\alpha L\mu + 3\alpha^2 L\mu^2)|k_2 a|^2 \varepsilon}{15\mu H^2 \mu(L - \mu^2)}. \quad (16)$$

According to equation (16), the value of  $Q_{\text{low}}^{-1}$  for penny-shaped cracks scales with the dimensionless frequency  $|k_2 a|^2$ . The logarithm of  $Q_{\text{low}}^{-1}$  for slit and penny-shaped cracks, according to equations (15) and (16), are also obtained

$$\begin{aligned} \log Q_{\text{low-2D}}^{-1} &= \log \left( \pi \varepsilon \frac{M(H - \alpha M)^2}{2\mu^2(\mu - H + \alpha M)^2} \right) + \log(|k_2 a|^2) \\ &+ \log \left[ \frac{1}{32} (\alpha\mu - 4L) \ln(|k_2 a|^2) + (Lc_1 - \alpha\mu c_2) \right], \end{aligned} \quad (17)$$

$$\log Q_{\text{low-3D}}^{-1} = \log(|k_2 a|^2) + \log \left[ \frac{2M(H - \alpha M)^2(2 - 4\alpha L\mu + 3\alpha^2 L\mu^2)\varepsilon}{15\mu H^2 \mu(L - \mu^2)} \right]. \quad (18)$$

To understand the behavior of  $Q_{\text{low}}^{-1}$  on bilogarithmic scale, we define

$$\omega = 10^x. \quad (19)$$

Then equations (17) and (18) can be transformed into

$$\log Q_{\text{low-2D}}^{-1} = \log Z + x + \log \left[ \frac{1}{32} \ln(10) \left( \frac{\alpha\mu}{L} - 4 \right) x - X \right], \quad (20)$$

$$\log Q_{\text{low-3D}}^{-1} = x + \log \left( \frac{bH}{LM} a^2 \right) + \log \left[ \frac{2M(H - \alpha M)^2(2 - 4\alpha L\mu + 3\alpha^2 L\mu^2)\varepsilon}{15\mu H^2 \mu(L - \mu^2)} \right], \quad (21)$$

with

$$Z = \pi n_0 a^2 \frac{M(H - \alpha M)^2}{(\mu - H + \alpha M)^2} \frac{L bH}{\mu LM} a^2, \quad (22)$$

and

$$X = \frac{1}{32} \left( \frac{\alpha\mu}{L} - 4 \right) \ln \left( \frac{bH}{LM} a^2 \right) + c_1 - \frac{\alpha\mu}{L} c_2. \quad (23)$$

Finally, calculating the low-frequency asymptotic solution for the derivative of  $\log Q_{\text{low}}^{-1}$  with respect to  $x$  for penny-shaped cracks gives

$$\frac{\partial [\log Q_{\text{low-3D}}^{-1}]}{\partial x} = 1, \quad (24)$$

and for slit cracks gives

$$\frac{\partial [\log Q_{\text{low-2D}}^{-1}]}{\partial x} = 1 + \frac{1}{x \ln^2(10) - \frac{32L \ln(10)X}{(-4L + \alpha\mu)}} = 1 - O \left( \frac{1}{\log(\omega)} \right). \quad (25)$$

Thus, we see that, indeed, in the limit of low frequencies, the slope  $\partial[\log(Q^{-1})]/\partial[\log(\omega)]$  tends to the same value of 1, but because of the presence of the logarithm in the asymptotic solution (25), for slit cracks, this limit is attained as a much slower rate than for penny-shaped cracks. The presence of the logarithm also explains the lack of straight line low-frequency asymptote for  $1/Q$  on bilogarithmic scale (just as a function  $\log(z)$  does not have a horizontal asymptote for  $z \rightarrow \infty$ , but  $d[\log(z)]/dz$  has a finite limit of zero).

#### 4.2. High-Frequency Asymptote

The high-frequency limit of  $f_{\text{high}}(0)$  is expressed as (see Appendix C)

$$f_{\text{high}}(0) = a^2 \sqrt{i} \frac{(H - \alpha M)^2}{2ML|k_2 a|}. \quad (26)$$

Combining equations (8) and (9) we get the high-frequency asymptotic analytical solutions for velocity and attenuation

$$v_{\text{high}}^* = \frac{v_1}{\left[1 + \frac{2\pi n_0}{k_1^2} \text{Re}\{f_{\text{high}}(0)\}\right]} = \frac{v_1}{1 + \frac{\sqrt{2}(H - \alpha M)^2 \varepsilon}{2ML|k_2 a|}} = v_1 \left[1 - \frac{\sqrt{2}}{2} \pi \frac{(H - \alpha M)^2 \varepsilon}{ML|k_2 a|}\right], \quad (27)$$

$$Q_{\text{high}}^{-1} = 4\pi n_0 \text{Im}[f_{\text{high}}(0)] = \sqrt{2} \pi \frac{(H - \alpha M)^2 \varepsilon}{ML|k_2 a|}, \quad (28)$$

shown as the black dashed lines in Figures 4a and 4b, respectively. Note that  $Q_{\text{high}}^{-1}$  is proportional to  $\omega^{-1/2}$ .

The analytical solution for  $P$  wave velocity and attenuation for penny-shaped crack in fluid saturated rocks at high frequencies has been derived by Galvin and Gurevich (2009):

$$v_{\text{high}}^* = v_1 \left[1 - \frac{\sqrt{2}}{2} \pi \frac{(H - \alpha M)^2 \varepsilon}{ML|k_2 a|}\right], \quad (29)$$

$$Q_{\text{high}}^{-1} = \sqrt{2} \pi \frac{(H - \alpha M)^2 \varepsilon}{ML|k_2 a|}. \quad (30)$$

Equations (27) and (28) are identical to equations (29) and (30), respectively. This confirms that the asymptotic behavior for the 2-D and 3-D cases at high frequencies is the same, which was also observed by Guo, Rubino, Barbosa, et al. (2018a), Guo, Rubino, Barbosa, et al. (2018b), and Guo, Rubino, Glubokovskikh, et al. (2018) by comparing the 2-D numerical simulations with the 3-D theoretical predictions. This is because at high frequencies the condition  $|k_2 a| \gg 1$  and the fluid diffusion length is much smaller than the crack length for both slit and penny-shaped cracks. Therefore, the shape of the crack does not affect overall properties. This behavior of attenuation at high frequencies is similar to the corresponding results for planar fractures of infinite extent (Gurevich et al., 2009) and for porous media with patchy saturation (Johnson, 2001).

#### 4.3. Cross-Over Frequency

The cross-over frequency represents the location of the attenuation peak and the largest slope for the dispersion due to the WIFF between the background medium and the fractures (Guo et al., 2017). Physically, the cross-over frequency corresponds to the situation where the fluid diffusion length is equal to the crack size. The cross-over frequency can be estimated by intersection of the low- and high-frequency asymptotic solutions (15) and (28),

$$\frac{\pi \varepsilon M (H - \alpha M)^2}{2\mu^2 (\mu - H + \alpha M)^2} |k_2 a|^2 \left[ \frac{1}{32} (4L - \alpha \mu) (\ln(|k_2 a|^2)) + (Lc_1 - \alpha \mu c_2) \right] = \sqrt{2} \pi \frac{(H - \alpha M)^2 \varepsilon}{ML|k_2 a|}. \quad (31)$$

By neglecting the slowly varying logarithmic term we obtain

$$\frac{\alpha M}{2(\mu - H + \alpha M)^2 \mu} \left( \frac{L}{\alpha \mu} c_1 - c_2 \right) |k_2 a|^2 = \frac{\sqrt{2}}{ML|k_2 a|}. \quad (32)$$

Because  $c_2$  is much smaller than  $(Lc_1/\alpha\mu)$ , it can be neglected so that

$$|k_2 a|^3 \approx \frac{\sqrt{2} (\mu - H + \alpha M)^2 \mu^2}{2 c_1 M^2 L^2}. \quad (33)$$

Using equation (33), we obtain the cross-over frequency  $\omega_c$  as

$$\omega_c = \left| \frac{k_2^2 LM}{bH} \right| = \frac{LM}{bHa^2} \left( \frac{\sqrt{2}(\mu - H + aM)^2 \mu^2}{2c_1 M^2 L^2} \right)^{\frac{2}{3}}. \quad (34)$$

Finally, we can estimate the peak value of attenuation by substituting the expression for  $\omega_c$  into the high-frequency asymptotic solution. This gives

$$Q_{\max}^{-1} = \sqrt{2} \frac{(H - aM)^2 \varepsilon}{ML} \left( \frac{2c_1 M^2 L^2}{\sqrt{2}(\mu - H + aM)^2 \mu^2} \right)^{\frac{1}{3}}. \quad (35)$$

For most of the rocks, we have  $aM \ll L$  and  $K_f \ll K_g$  and hence

$$Q_{\max}^{-1} \approx \left( \frac{4c_1 L^5 \phi}{(L - \mu)^2 \mu^2 K_f} \right)^{\frac{1}{3}} \varepsilon. \quad (36)$$

From equation (34), due to the fact that the value of the term  $\left[ \frac{\sqrt{2}(\mu - H + aM)^2 \mu^2}{2c_1 M^2 L^2} \right]$  is close to 1, the peak attenuation appears when the diffusion length is of the same order as the crack length. Equation (36) shows that the maximum attenuation is proportional to crack density (as it should be). Furthermore, it can be seen that peak attenuation increases with decreasing fluid bulk modulus, which is the same as for penny-shaped cracks (Galvin & Gurevich, 2009).

#### 4.4. Gassmann Consistency

In the low-frequency limit, the fluid in the fractures has enough time to communicate with that of the background pores and of other fractures, resulting in uniform fluid pressure throughout the pore and fracture space. Thus, the elastic properties of the saturated sample in the low-frequency limit should satisfy the anisotropic Gassmann equations (e.g., Brown & Korrington, 1975; Gassmann, 1951; Guo et al., 2017; Gurevich, 2003). The  $P$  wave modulus of the saturated fractured rock  $C_0$  in the direction perpendicular to the fracture plane in the low-frequency limit, according to equation (11), is given by

$$C_0 = H \left[ 1 - \frac{\pi(H - aM)^2 \varepsilon}{2\mu(H - \mu - aM)} \right]. \quad (37)$$

As shown in Appendix D, this result is consistent with anisotropic Gassmann equations.

Figure 4a shows that the  $P$  wave velocity for the slit crack case is somewhat lower than that for the penny-shaped cracks with the same crack density. The reason for this difference is the difference between the excess compliances caused by the same density of slit and penny-shaped cracks in an elastic medium. Indeed, the excess fracture compliances of the elastic medium with slit and penny-shaped cracks are given by equations (see e.g., Kachanov & Sevostianov, 2005)

$$Z_N = \frac{\pi \varepsilon L}{2\mu(L - \mu)}$$

and

$$Z_N = \frac{4\varepsilon L}{3\mu(L - \mu)}$$

respectively. This shows that the excess normal compliance caused by slit cracks is larger than for penny-shaped cracks by a factor  $3\pi/8 \approx 1.18$ . This difference manifests itself in the difference in dry  $P$  wave moduli and hence also the saturated moduli (as per anisotropic Gassmann equations) for the two cases.

### 5. Branching Function Approximation

While the dispersion and attenuation can be obtained by numerical methods, as shown in Figure 4, no corresponding explicit expressions have been derived. Such a solution would be very useful for practical

purposes, especially if the model is used to invert laboratory or field data for fracture parameters. One way to derive such a solution is to follow the approach of Johnson (2001). As suggested by Johnson (2001), the complex modulus of a material with mesoscopic fluid flow can be approximated by a simple branching function, if we know the asymptotic solutions at low and high frequencies. This approach was used by Gurevich et al. (2009) for the aligned penny-shaped crack and planar fracture cases with infinitesimal fracture thickness and was extended to finite thickness penny-shaped cracks by Guo, Rubino, Barbosa, et al. (2018a) and Guo, Rubino, Barbosa, et al. (2018b).

For slit cracks, to describe the frequency-dependent  $P$  wave modulus  $C_{22}^{\text{sat}}$  in the direction perpendicular to the fracture plane due to WIFF between the fractures and the background, we suggest the following form of the branching function (Gurevich et al., 2009)

$$\frac{1}{C_{22}^{\text{sat}}} = \frac{1}{H} \left[ 1 + \left( \frac{H - C_0}{C_0} \right) / \left( 1 - \zeta + \zeta \sqrt{1 - \frac{i\omega\tau}{\zeta^2}} \right) \right], \quad (38)$$

where  $C_0$  is the  $P$  wave modulus of the saturated fractured rock in the direction perpendicular to the fracture plane in the low-frequency limit (equation (37)).

The behavior of the attenuation and dispersion in equation (38) is controlled by two parameters:  $\zeta \geq 0$  and  $\tau > 0$ . Parameter  $\zeta$  controls the shape of the attenuation and dispersion curves, while  $\tau$  defines the time scale. Equation (38) shows, in general, up to three different attenuation/dispersion regimes:

$$\frac{1}{C_{22}^{\text{sat}}} = \frac{1}{C_0} (1 + i\omega T), \quad \omega\tau \ll \zeta^2, \quad (39)$$

$$\frac{1}{C_{22}^{\text{sat}}} = \frac{1}{C_0} \left( 1 - F\sqrt{-i\omega} \right), \quad \zeta^2 \ll \omega\tau \ll 1, \quad (40)$$

and

$$\frac{1}{C_{22}^{\text{sat}}} = \frac{1}{H} \left( 1 + \frac{G}{\sqrt{-i\omega}} \right), \quad \omega\tau \gg 1. \quad (41)$$

It can be seen from equations (39) and (41) that the attenuation at low and high frequencies is controlled by  $T$  and  $G$ , respectively. The time scaling parameter  $\tau$  and shape parameter  $\zeta$  are then related to the low- and high-frequency scaling coefficients  $T$  and  $G$  by

$$\tau = \left( \frac{H - C_0}{HG} \right)^2, \quad (42)$$

$$\zeta = \frac{(H - C_0)^3}{2C_0 H^2 T G^2}. \quad (43)$$

According to equations (15), we have the following analytical expression for  $C_{22}^{\text{sat}}$  at low frequencies:

$$\frac{1}{C_{22}^{\text{sat}}(\omega)} = \frac{1}{C_0} \left[ 1 + (k_2 a)^2 \pi \varepsilon \frac{M(H - aM)^2}{2\mu^2(\mu - H + aM)^2} \times \left[ \frac{1}{32} (a\mu - 4L) \ln(|k_2 a|^2) + (LC_1 - a\mu c_2) \right] \right], \quad \omega\tau \ll \zeta^2. \quad (44)$$

where  $C_0$  is the value of  $C_{22}^{\text{sat}}$  in the low-frequency limit, as shown in equation (37).

Since the low-frequency asymptotic solution does not scale with frequency, it cannot be described by equation (44). However, as discussed in section 4.1 (see Figure 4b), while the attenuation factors at low frequencies for the slit and penny-shaped crack cases have some differences, these differences are only

significant for very low frequencies, where attenuation is negligible. Due to the fact that the attenuation at low frequencies is determined by the value of  $T$ , the expression for  $T$  for the slit crack case can thus be approximated by that for the penny-shaped crack case as follows:

$$T \approx \frac{2(H - \alpha M)^2 (2 - 4\alpha g + 3\alpha^2 g^2) a^2 \varepsilon b}{15\mu g (1 - g)^2 HL}, \quad (45)$$

and

$$g = \frac{\mu}{L}. \quad (46)$$

At high frequencies, from equations (27) and (28), we have

$$\frac{1}{c_{22}^{\text{sat}}(\omega)} = \frac{1}{H} \left[ 1 + \frac{2\sqrt{MLb/H\pi(H - \alpha M)^2 \varepsilon}}{LM\sqrt{-i\omega a}} \right], \quad \omega\tau \gg 1. \quad (47)$$

Comparing equation (41) with (47), we obtain  $G$ , as follows:

$$G = \frac{2\pi\varepsilon}{a} (H - \alpha M)^2 \sqrt{\frac{1}{HMLb}}. \quad (48)$$

Substituting equations (45), (46), and (48) into (42) and (43) and substituting equations (42) and (43) into (38), we finally obtain the explicit expression for the  $P$  wave modulus  $C_{22}^{\text{sat}}$  for the slit crack case using the branching function approach. The results are shown in Figures 4a and 4b, by the black solid lines. We see that the results given by the branching function are in a very good agreement with the numerical simulations and only begin to deviate at very low frequencies, where attenuation is negligible anyway.

## 6. Discussion

In this paper, we considered the dispersion and attenuation due to WIFF in saturated porous rocks with aligned slit cracks. The results show that the characteristics of the seismic dispersion and attenuation for the slit cracks are similar to those for the penny-shaped cracks. At high frequencies, the analytical solutions for the seismic dispersion and attenuation for the slit crack case are identical with those for the penny-shaped crack case. At low frequencies, while the velocities in these two cases are slightly different, the behavior of attenuation factors is similar. These observations are consistent with those of Guo, Rubino, Barbosa, et al., (2018a), Guo, Rubino, Barbosa, et al., (2018b), and Guo, Rubino, Glubokovskikh, et al., (2018), which found that the 3-D (penny-shaped cracks) theoretical predictions are in good agreement with the 2-D (slit cracks) numerical simulations after scaling the elastic moduli in the low- and high-frequency limits. Similar conclusions are also drawn by Barbosa et al. (2017) and Hunziker et al. (2018) through the comparison of the 2-D and 3-D numerical simulations for the aligned fracture cases. The comparison of the theoretical models for the slit and penny-shaped cracks in this paper confirms that the seismic dispersion and attenuation due to WIFF for waves perpendicular to fractures are relatively insensitive to the largest dimension ("length") of the fractures.

The results of the present work and Galvin and Gurevich (2009) give the complete solution for dispersion and attenuation due to wave-induced flow between pores and fractures for a single set of parallel slit and circular cracks, respectively. More complex geometries such as two sets of intersecting cracks still require numerical simulations (Rubino et al., 2014). However, Guo et al. (2017) and Guo, Rubino, Glubokovskikh, et al., (2018) showed that the numerical results can be approximated analytically using a combination of solutions for single sets of cracks.

In this paper we assumed that the wave frequency is below the Biot's crossover frequency, and hence, the wave propagation is in the low-frequency regime of Biot theory (Biot, 1956a). Furthermore, the cracks were assumed to be much smaller than the seismic wavelength, so that the scattering effects are negligible. Despite this, the fluid diffusion effects may still be significant because cracks can be comparable in size to the wavelength of the Biot slow wave (fluid diffusion length), which, in Biot's low-frequency regime, is

much smaller than the wavelength of the fast compressional or shear wave. It may be possible to extend our formulation to the higher frequency range of Biot's theory (1956b; see Hefner and Jackson, 2014). However at those frequencies the wavelengths of the fast and slow waves are comparable, and hence, if the crack length is comparable to the wavelength of the slow wave, it is also comparable to the wavelength of the fast one. Thus, the pressure diffusion effects are likely to be overshadowed by the scattering effects.

## 7. Conclusions

Using the solutions for the single slit crack scattering and multiple-scattering theory, we estimated the attenuation and velocity dispersion of elastic waves in a porous medium containing a sparse distribution of aligned slit cracks. We obtained numerical solutions for the entire frequency range and asymptotic analytical solutions at low and high frequencies. In addition, we derived the expression for the cross-over frequency where the maximum attenuation and dispersion occur. The results show that the maximum attenuation occurs when the diffusion length is of the order of the crack size. The peak frequency decreases with increasing crack radius.

When comparing the results for the slit crack case with those for the penny-shaped crack case, we find that the characteristics of the seismic dispersion and attenuation for these two cases are similar. At high frequencies, the fluid diffusion length is much smaller than the crack length for both slit and penny-shaped crack cases. Therefore, the geometric influence of the crack can be neglected. Media that have the same background properties and crack density will have the same velocities and attenuation factors. Conversely at low frequencies, due to the different geometries of the slit and penny-shaped cracks, the characteristics of seismic dispersion and attenuation are somewhat different. The slope of attenuation factor versus frequency curve on bilogarithmic scale for both penny-shaped and slit cracks tends to 1. However, for slit cracks, the slope for approaches the asymptotic value of 1 much slower than for penny-shaped cracks. This difference manifests itself in somewhat different behavior of  $1/Q$  versus frequency. For penny-shaped cracks, attenuation has a low-frequency asymptote  $Q^{-1} \propto \omega$ . However, no such asymptote is observed for slit cracks, as the asymptotic solution is logarithmic.

Similarly to the penny-shaped cracks, calculation of the velocity and attenuation as functions of frequency for slit cracks requires numerical solution of an integral equation, while analytical solutions are only obtained for very low and very high frequencies (with respect to the pressure diffusion effects). However, we have also proposed a closed-form approximation for the entire frequency range. The results given by the branching function are in good agreement with the numerical results. This approximation is given by a very simple equation and may be useful for estimation of fracture parameters from laboratory or field data, or for comparison with numerical simulations.

## Appendix A: The Solution of Scattering by a Single Crack

### A1. Equations of Poroelasticity

The solid and relative fluid displacements in response to stress are described by Biot's dynamic poroelasticity equations (Biot, 1962) in the space-frequency domain,

$$\nabla \cdot \sigma = -\omega^2 (\rho \vec{u} + \rho_f \vec{w}), \nabla p = -\omega^2 (\rho_f \vec{u} + q \vec{w}), \quad (\text{A1})$$

where  $\vec{w} = \phi(\vec{U} - \vec{u})$  is the relative fluid displacement,  $\vec{u}$  is the solid displacement,  $\vec{U}$  is the average absolute fluid displacement of the pore fluid, and  $\phi$  is the total porosity of the background medium.  $\omega$  is the angular frequency,  $\sigma$  is the total stress tensor, and  $p$  is the fluid pressure.  $\rho_f$  and  $\rho$  are the densities of the fluid and of the overall medium, respectively. The parameter  $q$  is a frequency-dependent coefficient responsible for viscous and inertial coupling between the solid and fluid displacements. We assume that the fractures are mesoscopic, that is, much larger than the pore size but much smaller than the wavelengths of fast compressional and shear waves (Galvin & Gurevich, 2007, 2009; Guo, Rubino, Barbosa, et al., 2018a). Since seismic frequencies are always much smaller than Biot's critical frequency, the fluid flow in the pores is the Poiseuille type and  $q(\omega) = i\eta/\kappa\omega$  (Biot, 1956a), where  $\kappa$  is the rock permeability and  $\eta$  is the shear viscosity.

Following Biot (1962), the constitutive relations are written in the form

$$\sigma = [(H - 2\mu)\nabla\vec{u} + \alpha M\nabla\vec{w}]I + \mu[\nabla\vec{u} + (\nabla\vec{u})^T], p = -\alpha M\nabla\vec{u} - M\nabla\vec{w}. \quad (\text{A2})$$

In equation (A2),  $\mu$  is the shear modulus of the solid frame and  $\alpha = 1 - K_d/K_g$  is the Biot-Willis coefficient (Biot & Willis, 1957). The coefficient  $K_d$  is the bulk modulus of the dry rock frame,  $K_g$  is the bulk modulus of the solid grain material, and  $M$  is the pore space modulus, given by

$$M = \left[ \frac{(\alpha - \phi)}{K_g} + \frac{\phi}{K_f} \right]^{-1}, \quad (\text{A3})$$

where  $K_f$  is the bulk modulus of pore fluid

$$H = K_{\text{sat}} + \frac{4}{3}\mu, \quad (\text{A4})$$

is the  $P$  wave modulus of the saturated poroelastic medium.  $K_{\text{sat}}$  is the undrained bulk modulus of the fluid saturated rock, which is expressed by the Gassmann equation (Gassmann, 1951)

$$K_{\text{sat}} = K_d + \alpha^2 M. \quad (\text{A5})$$

To determine the equations governing the propagation of the dilatational and shear waves in the  $x$ - $y$  plane under the state of plane strain, the equations of motion (A1) should be decomposed into dilatational and shear wave equations by expressing the displacement vectors as follows, according to Helmholtz's potential theory (e.g., Achenbach, 2012; Song et al., 2017a, 2017b),

$$\begin{aligned} \vec{u} &= \nabla\Phi_1 + \Phi_2 + \nabla \times \vec{\psi}, \\ \vec{w} &= \chi_1 \nabla\Phi_1 + \chi_2 \nabla\Phi_2 + \chi_3 \nabla \times \vec{\psi}. \end{aligned} \quad (\text{A6})$$

In equation (A6),  $\Phi_1$  and  $\Phi_2$  are the scalar potentials for the  $P_1$  (fast) and the  $P_2$  (slow) waves. The vector potential  $\vec{\psi}$  refers to the  $S$  wave (shear wave). At low frequencies, the  $P_1$  wave propagates with small attenuation and velocity dispersion, while the  $P_2$  wave is highly attenuated and is governed by a diffusion equation. The coefficients  $\chi_i$  ( $i = 1, 2, 3$ ) denote the amplitude ratios of relative fluid displacements and solid displacements in corresponding wave modes. For frequencies lower than Biot's critical frequency, they are given as

$$\chi_1 = -\frac{[i\omega(\alpha M\rho - H\rho_f)]}{bH} \approx 0, \quad \chi_2 = -\frac{H}{\alpha M}, \quad \chi_3 = \frac{i\rho_f \kappa \omega}{\eta}. \quad (\text{A7})$$

Using equations (A2) and (A6), we can therefore decompose equation (A1) into scalar equations in the coordinates  $(x, y)$ . Their expressions are given as

$$(\nabla^2 + k_i^2)\Phi_i = 0, \quad i = 1, 2, \quad (\nabla^2 + k_3^2)\vec{\psi} = 0, \quad (\text{A8})$$

where  $k_1$  and  $k_2$  are the wave numbers of  $P_1$  (fast) wave and  $P_2$  (slow) waves.  $k_3$  is the wave number of the  $S$  wave. They are expressed as

$$k_1 = \sqrt{\frac{\rho\omega^2}{H}}, \quad k_2 = \sqrt{\frac{ibH\omega}{LM}}, \quad k_3 = \sqrt{\frac{\rho\omega^2}{\mu}}, \quad (\text{A9})$$

where  $b = \eta/\kappa$ .  $L = K_d + 4/3\mu$  is the  $P$  wave modulus of the solid rock frame.

## A2. Boundary Conditions

For the plane strain problem shown in section 2.1 (Figure 3), due to the infinitesimal thickness of the crack, the scattered displacement vectors should be symmetric about the  $x$  axis (Figure 3). Therefore, the boundary conditions can be formulated in the upper half plane, that is,  $y \geq 0$ .

First, the scattered displacement vectors should be symmetric about the  $x$  axis, which requires that the scattered shear stress and the scattered normal component of the solid and fluid displacements must be zero, on  $y = 0$  for  $|x| > a$  (e.g., Galvin & Gurevich, 2007; Song et al., 2017b),

$$\sigma_{xy}^{(s)}(x, 0) = 0, \quad u_y^{(s)}(x, 0) = 0, \quad w_y^{(s)}(x, 0) = 0. \quad (\text{A10})$$

In general, the cracks are in hydraulic communication with the surrounding porous medium. For a fluid-filled permeable crack, there are no shear tractions acting on the surface, and the continuity of the normal traction requires that the normal stress is equal to the negative of the fluid pressure in the crack. In this way, the following stress boundary conditions are obtained, on  $y = 0$  for  $|x| \leq a$ ,

$$\sigma_{xy}^{(s)}(x, 0^+) + \sigma_{xy}^{(i)}(x, 0^+) = 0, \quad \sigma_{yy}^{(s)}(x, 0^+) + \sigma_{yy}^{(i)}(x, 0^+) = -p(x, 0^+). \quad (\text{A11})$$

Following Hudson (1981) and Galvin and Gurevich (2007), the crack-filling fluid can be regarded as incompressible, if

$$\frac{K_f}{\mu} \gg \frac{c}{a}. \quad (\text{A12})$$

For the crack with an infinitesimal thickness ( $c \approx 0$ ,  $c/a \approx 0$ ), the displacements on the crack surface should satisfy

$$u_y^{(s)}(x, 0^+) + w_y^{(s)}(x, 0^+) = 0, \quad |x| \leq a. \quad (\text{A13})$$

The incident displacement  $\bar{u}^{-i}$  and stress  $(\sigma_{yy}^{(i)} \sigma_{xx}^{(i)} \sigma_{xy}^{(i)} p^{(i)})$  are given as

$$\begin{pmatrix} u_y^{(i)} \\ w_y^{(i)} \\ \sigma_{yy}^{(i)} \\ p^{(i)} \end{pmatrix} = u_0 \begin{pmatrix} 1 \\ \chi_1 \\ ik_1 H \\ -ik_1 (\alpha M) \end{pmatrix} e^{-ik_1 y}, \quad (\text{A14})$$

Other components  $(u_x^{(i)} w_x^{(i)} \sigma_{xx}^{(i)} \sigma_{xy}^{(i)})$  vanish.

Combining equations (A10), (A11), (A13), and (A14), because the crack is also symmetric about  $y$  axis, the boundary conditions can be reformulated, in the first quartile in the  $x$ - $y$  plane, as

$$\begin{aligned} \sigma_{xy}^{(s)}(x, 0) = 0, \quad x \geq 0, \quad u_y^{(s)}(x, 0) + w_y^{(s)}(x, 0) = 0, \quad x \geq 0, \quad u_y^{(s)}(x, 0) = 0, \quad x > a, \quad \sigma_{yy}^{(s)}(x, 0) + p^{(s)}(x, 0) \\ = -\sigma_{yy}^{(i)}(x, 0) - p^{(i)}, \quad x \leq a. \end{aligned} \quad (\text{A15})$$

### A3. Solution of the Scattering Field of Single Crack

Combining Biot's poroelastic equation and boundary conditions, we can obtain the scattered displacement fields as (Song et al., 2017b)

$$\begin{aligned} u_y^{(s)}(x, y) &= -\frac{2}{\pi} \int_0^\infty [\sum_{i=1}^2 A_i(k) \eta_i e^{-\eta_i y} + A_3(k) k e^{-\eta_3 y}] \cos(kx) dk, \\ w_y^{(s)}(x, y) &= -\frac{2}{\pi} \int_0^\infty [\sum_{i=1}^2 \chi_i A_i(k) \eta_i e^{-\eta_i y} + \chi_3 A_3(k) k e^{-\eta_3 y}] \cos(kx) dk, \\ u_x^{(s)}(x, y) &= -\frac{2}{\pi} \int_0^\infty [\sum_{i=1}^2 A_i(k) k e^{-\eta_i y} + A_3(k) \eta_3 e^{-\eta_3 y}] \sin(kx) dk, \\ w_x^{(s)}(x, y) &= -\frac{2}{\pi} \int_0^\infty [\sum_{i=1}^2 \chi_i A_i(k) k e^{-\eta_i y} + \chi_3 A_3(k) \eta_3 e^{-\eta_3 y}] \sin(kx) dk, \end{aligned} \quad (\text{A16})$$

with

$$A_3(k) = \frac{-2k[A_1(k)\eta_1 + A_2(k)\eta_2]}{2k^2 - k_3^2}, \quad A_2(k) = \frac{\chi_3 - \chi_1 k^2 - \sigma_4 k_2^2 \eta_1}{\chi_3 - \chi_2 k^2 - \sigma_3 k_1^2 \eta_2} A_1(k), \quad (\text{A17})$$

where  $k$  is the radial wave number of scattered wave and  $\eta_i = \sqrt{k^2 - k_i^2}$  is the axial wave number. According to equations (A16) and (A17), if we get the expression of  $A_1(k)$  (the displacement potential amplitude in wave number domain in  $x$  direction), we can get the scattered displacement field.

Song et al. (2017b) showed that  $A_1(k)$  is related to an unknown function  $B(k)$ ,

$$A_1(k) = \frac{\pi(\chi_3 - \chi_2)(k^2 - \sigma_3 k_1^2)B(k)}{E\eta_1}. \quad (\text{A18})$$

In equation (A18), the only unknown function  $B(k)$  is determined by a pair of dual integral equations,

$$\int_0^\infty k[1 + H(k)]B(k) \cos(kx)dk = -f_0, 0 \leq x \leq a, \int_0^\infty B(k) \cos(kx)dk = 0, x > a, \quad (\text{A19})$$

with

$$H(k) = \frac{4\mu}{Ek}(\chi_3 - \chi_2)(k^2 - \sigma_1 k_1^2)(k^2 - \sigma_3 k_1^2) \frac{1}{\eta_1} + \frac{4\mu}{Ek} \left[ (\chi_1 - \chi_3)(k^2 - \sigma_2 k_2^2)(k^2 - \sigma_4 k_2^2) \frac{1}{\eta_2} - (\chi_1 - \chi_2)k^2 \eta_3 \right] - 1, \quad (\text{A20})$$

$$E = 2\mu k_3^2 \frac{\mu - H + aM}{aM}, \quad (\text{A21})$$

and

$$\begin{aligned} \sigma_1 &= \frac{H - aM}{2\mu}, \\ \sigma_2 &= \frac{L}{2a\mu}, \\ \sigma_3 &= \frac{H - aM}{2\mu}, \\ \sigma_4 &= \frac{ML\rho}{2H\mu\rho_i}. \end{aligned} \quad (\text{A22})$$

Dual integral equation (A19) can be reduced to a single Fredholm equation of the second kind (e.g., Galvin & Gurevich, 2007; Song et al., 2017b):

$$B(k) + \int_0^\infty R(k, k')H(k')B(k')dk' = -f_0S(k), \quad (\text{A23})$$

where

$$R(k, k') = ak' \left[ \frac{k'J_{-1}(k'a)J_0(ka) - kJ_{-1}(ka)J_0(k'a)}{k^2 - k'^2} \right], \quad (\text{A24})$$

$$S(k) = ak^{-1}J_1(ka), \quad (\text{A25})$$

$$f_0 = ik_1(H - aM) \quad (\text{A26})$$

and  $J_1(ka)$  is the first-order Bessel function.  $k$  and  $k'$  are radial wave numbers. By solving the Fredholm integral equation (A23), we can get the function  $B(k)$  and hence define the parameters of scattering field produced by the fracture.

## Appendix B: Far-Field Scattering Amplitude

The use of Waterman-Truell approximation requires  $f(0)$ , the far-field scattering amplitude of the fast-compressional wave for a single crack in the direction of the incident wave. Since the incident wave approaches along the  $y$  direction

$$f(0) = \lim_{y \rightarrow \infty} u_y(0, y). \quad (\text{B1})$$

where  $u_y(0, y)$  is given by the fast wave ( $i = 1$ ) term in equation (A16). When  $y$  tends to  $\infty$ ,  $u_y^{(s)}(0, y)$  can be approximated as follows:

$$\begin{aligned} f(0) &= \lim_{y \rightarrow \infty} u_y(0, y) = \frac{-2}{\pi} \lim_{y \rightarrow \infty} \int_0^{\infty} A_1(k) \sqrt{k^2 - k_1^2} e^{-\sqrt{k^2 - k_1^2} y} dk \\ &= \frac{-2i}{\pi} \lim_{y \rightarrow \infty} \int_0^{k_1} A_1(k) \sqrt{k_1^2 - k^2} e^{-i\sqrt{k_1^2 - k^2} y} dk - \frac{2}{\pi} \lim_{y \rightarrow \infty} \int_{k_1}^{\infty} A_1(k) \sqrt{k^2 - k_1^2} e^{-\sqrt{k^2 - k_1^2} y} dk, \end{aligned} \quad (B2)$$

where the second term in the right-hand side tends to zero, due to the presence of the negative exponential term. Finally,  $f(0)$  can be expressed as

$$f(0) = \lim_{y \rightarrow \infty} u_y(0, y) = \frac{-2i}{\pi} \lim_{y \rightarrow \infty} \int_0^{k_1} A_1(k) \sqrt{k_1^2 - k^2} e^{-i\sqrt{k_1^2 - k^2} y} dk. \quad (B3)$$

To calculate the infinite limit, we make

$$\sqrt{k_1^2 - k^2} y = 2\pi n, n \in \mathbb{Z}, \quad (B4)$$

and

$$y = \frac{2\pi n}{\sqrt{k_1^2 - k^2}}. \quad (B5)$$

Therefore, we have

$$\lim_{n \rightarrow \infty} y = \infty, \quad (B6)$$

as well as

$$f(0) = \lim_{y \rightarrow \infty} u_y(0, y) = \frac{-2i}{\pi} \int_0^{k_1} A_1(k) \sqrt{k_1^2 - k^2} dk. \quad (B7)$$

We make the transformation below:

$$k = k_1 \sin \theta, 0 \leq \theta \leq \frac{\pi}{2}. \quad (B8)$$

Substituting equation (B8) into (B7), we obtain

$$f(0) = \lim_{y \rightarrow \infty} u_y(0, y) = -\frac{2i}{\pi} \int_0^{\frac{\pi}{2}} A_1(k_1 \sin \theta) k_1^2 \cos^2 \theta d\theta \approx -\frac{2i}{\pi^2} A_1(0) k_1^2 \int_0^{\pi} \frac{\cos \theta + 1}{2} d\theta = -\frac{i}{\pi} A_1(0) k_1^2. \quad (B9)$$

## Appendix C: Derivation of the Asymptotic Results

### C1. Low-Frequency Asymptote

At low frequencies, due to the large fluid-diffusion length,  $|k_2 a| \ll 1$ , and kernel function  $H(k')$  only contributes significantly to the integral in equation (A23) for  $k'$  of the order  $1/a$  (Galvin & Gurevich, 2009). For  $k' \ll 1/a$ ,  $S(k')$  is small. Thus,  $H(k')$  only contributes to the integral in equation (A23) for  $k' \gg |k_2|$ , and the low-frequency approximation of  $H(k')$  can be obtained as

$$\begin{aligned} H_{\text{low}}(k') &= \frac{4\mu}{E} (\chi_3 - \chi_2) \left[ \left[ \frac{1}{2} - (\sigma_1 + \sigma_3) \right] k_1^2 \right] + \frac{4\mu}{E} (\chi_1 - \chi_3) \left[ -(\sigma_2 + \sigma_4) \frac{k' k_2^2}{\eta_2} + (\sigma_2 \sigma_4) \frac{k_2^4}{\eta_2 k'} \right] \\ &\quad + \frac{4\mu}{E} (\chi_1 - \chi_2) \frac{k_3^2}{2} - 1. \end{aligned} \quad (C1)$$

In the low-frequency limit, the contribution of the integral in equation (A23) is small, and thus, equation (A23) can be solved by iteration. We assume an initial solution as follows:

$$B(k') \approx -f_0 S(k'), \quad (C2)$$

Then substitution of equations (C1) and (C2) into (A23) yields

$$B_{low}(k) = f_0 \int_0^\infty R(k, k') H_{low}(k') S(k') dk' - f_0 S(k). \quad (C3)$$

Hence,  $B_{low}(0)$  can be written as

$$B_{low}(0) = f_0 \int_0^\infty \lim_{k \rightarrow 0} R(k, k') H_{low}(k') S(k') dk' - f_0 \lim_{k \rightarrow 0} S(k), \quad (C4)$$

with

$$\lim_{k \rightarrow 0} R(k, k') = \lim_{k \rightarrow 0} \left\{ ak' \left[ \frac{k' J_{-1}(k'a) J_0(ka) - k J_{-1}(ka) J_0(k'a)}{k^2 - k'^2} \right] \right\} = a J_1(k'a), \quad (C5)$$

and

$$\lim_{k \rightarrow 0} S(k) = \lim_{k \rightarrow 0} [ak^{-1} J_1(ka)] = \frac{1}{2} a^2. \quad (C6)$$

Substituting equations (C5) and (C6) into (C4), upon evaluation of the integral (C4), we obtain

$$\begin{aligned} B_{low}(0) &= f_0 a^2 \int_0^\infty H_{low}(k') [J_1(k'a)] \frac{J_1(k'a)}{k'} dk' - \frac{1}{2} a^2 f_0 \\ &= f_0 a^2 \frac{\alpha M}{2(\mu - H + \alpha M)} \times \left[ \frac{H - \mu - \alpha M}{\alpha M} - \frac{1}{2} \text{ilm} \left( \int_0^\infty \frac{J_1^2(x)}{\sqrt{x^2 - (k_2 a)^2}} dx \right) + \frac{L}{\alpha \mu} k_2^2 a^2 \int_0^\infty \frac{J_1^2(x)}{x^2 \sqrt{x^2 - (k_2 a)^2}} dx \right]. \end{aligned} \quad (C7)$$

Substituting equation (C7) into (4), we have

$$\begin{aligned} f_{low}(0) &= \frac{(H - \alpha M)^2}{8\mu(H - \mu - \alpha M)} a^2 \\ &+ \frac{\alpha M(H - \alpha M)^2}{8\mu(\mu - H + \alpha M)^2} \left[ \left( \frac{L}{\alpha \mu} \right) k_2^2 a^2 \int_0^\infty \frac{J_1^2(x)}{x^2 \sqrt{x^2 - (k_2 a)^2}} dx - \frac{1}{2} \text{ilm} \left( \int_0^\infty \frac{J_1^2(x)}{\sqrt{x^2 - (k_2 a)^2}} dx \right) \right]. \end{aligned} \quad (C8)$$

## C2. High-Frequency Asymptote

At high frequencies,  $|k_2 a| \gg 1$ , this means that functions  $R(k, k')$  and  $H(k')$  as given by equations (A20) and (A24) are functions oscillating with a period of  $2\pi/a$  and decaying with a positive power of  $k'$  (Galvin & Gurevich, 2009). When  $k'$  is high enough,  $H(k')$  will be equal to zero. Thus, the integration from 0 to  $k_0'$  contributes most to the integral in equation (A23), which means equation (A23) can be approximated as follows:

$$B_{high}(k) + \int_0^{k_0'} R(k, k') H(k') B(k') dk' = -f_0 S(k), \quad (C9)$$

where  $k_0'$  is on the order of  $1/a$ . At high frequency,  $|k_2| \gg k' \gg k_3 > k_1$ , and the terms  $k'/k_2$ ,  $k_3/k'$ , and  $k_1/k'$  can be neglected. Thus, the function  $H(k')$  can be simplified as

$$H_{high}(k') = \frac{4\mu}{Ek'} \left[ i(\chi_3 - \chi_1) [((\sigma_2 \sigma_4) k_2^4)] \frac{1}{\sqrt{k_2^2}} \right] - 1. \quad (C10)$$

Substituting equation (C10) into dual integral equation (A19) yields

$$\int_0^{\infty} B_{\text{high}}(k) \cos(kx) dk = -\frac{E\sqrt{k_2^2 f_0}}{4\mu [i(\chi_3 - \chi_1) [((\sigma_2 \sigma_4) k_2^4)]]}, 0 \leq x \leq a, \int_0^{\infty} B_{\text{high}}(k) \cos(kx) dk = 0, x > a. \quad (\text{C11})$$

Dual integral equation (C11) is equivalent to a single integral equation for  $B_{\text{high}}(k)$ :

$$\int_0^{\infty} B_{\text{high}}(k) \cos(kx) dk = D(x), \quad (\text{C12})$$

where

$$D(x) = \begin{cases} a \frac{E\sqrt{k_2^2 f_0}}{4\mu [i(\chi_3 - \chi_1) [((\sigma_2 \sigma_4) k_2^4)]]}, & 0 \leq x \leq a, \\ 0, & x > a. \end{cases} \quad (\text{C13})$$

In equation (C13), the left-hand side is the cosine transform of the function  $B_{\text{high}}(k)$ . Then, the function  $B_{\text{high}}(k)$  can be computed using the inverse cosine transform of the right-hand side,

$$\begin{aligned} B_{\text{high}}(k) &= \int_0^{\infty} D(x) \cos(kx) dx = a \frac{E\sqrt{k_2^2 f_0}}{4\mu [i(\chi_3 - \chi_1) [((\sigma_2 \sigma_4) k_2^4)]]} \int_0^a \cos(kx) dx \\ &= a \frac{E\sqrt{k_2^2 f_0} \sin(ak)}{4\mu [i(\chi_3 - \chi_1) [((\sigma_2 \sigma_4) k_2^4)]]} k. \end{aligned} \quad (\text{C14})$$

For the far-field scattering, we only need the value of  $B_{\text{high}}(0)$

$$B_{\text{high}}(0) = a \frac{E\sqrt{k_2^2 f_0}}{4\mu [i(\chi_3 - \chi_1) (\sigma_2 \sigma_4) k_2^4]} \lim_{k \rightarrow 0} \frac{\sin(ak)}{k} = -\frac{2a^2 f_0 \mu^2 k_3^2 (\mu - H + \alpha M) \sqrt{i}}{M[(L\rho\omega^2 |k_2|)]}. \quad (\text{C15})$$

Substitution of equation (C15) into (4) yields

$$f_{\text{high}}(0) = \frac{(H - \alpha M) H k_1}{2(\mu - H + \alpha M) \mu^2 k_3^2} B_{\text{high}}(0) = a^2 \sqrt{i} \frac{(H - \alpha M)^2}{2ML|k_2 a|}. \quad (\text{C16})$$

#### Appendix D: P Wave Modulus $C_{22}^{\text{sat}}$ in the Low-Frequency Limit

In the low-frequency limit, the fluid pressure in the fractures has enough time to communicate with that in the background medium. Hence, we can use the Gassmann equation to calculate the elastic properties of the saturated fractured rock. In order to do so, first we need to obtain the elastic properties for the dry fractured rock. This can be done by using the linear slip theory (Schoenberg & Sayers, 1995) as follows:

$$S^0 = S^b + S^c, \quad (\text{D1})$$

where  $S^0$  is the compliance of the fractured rock and  $S^b$  and  $S^c$  are the compliance matrix of the background medium and the fractures, respectively.

$S^b$  can be represented by

$$S^b = \begin{bmatrix} A & 0 \\ 0 & B \end{bmatrix}, \quad (\text{D2})$$

with

$$A = \begin{bmatrix} 1/E_b & -\nu_b/E_b & -\nu_b/E_b \\ -\nu_b/E_b & 1/E_b & -\nu_b/E_b \\ -\nu_b/E_b & -\nu_b/E_b & 1/E_b \end{bmatrix}, B = \begin{bmatrix} 2(1 + \nu_b)/E_b & 0 & 0 \\ 0 & 2(1 + \nu_b)/E_b & 0 \\ 0 & 0 & 2(1 + \nu_b)/E_b \end{bmatrix}, \quad (\text{D3})$$

where  $E_b$  and  $\nu_b$  are Young's modulus and Poisson's ratio of the dry background medium, respectively, represented as (Mavko et al., 2009)

$$E_d = \frac{9K_d\mu}{3K_d + \mu}, \quad \nu_b = \frac{3K_d - 2\mu}{2(3K_d + \mu)}, \quad K_d = L - \frac{4}{3}\mu. \quad (D4)$$

$S^c$  is given as

$$S^c = \begin{bmatrix} P & 0 \\ 0 & U \end{bmatrix}, \quad (D5)$$

with

$$P = \begin{bmatrix} 0 & 0 & 0 \\ 0 & Z_N & 0 \\ 0 & 0 & 0 \end{bmatrix}, \quad U = \begin{bmatrix} 0 & 0 & 0 \\ 0 & Z_{T2} & 0 \\ 0 & 0 & Z_{T1} \end{bmatrix}, \quad (D6)$$

Here we only concentrate on the  $P$  wave modulus, which is only related to  $Z_N$ . Hence, we only need the expression of  $Z_N$  as follows (Guo et al., 2017; Kachanov & Sevostianov, 2005):

$$Z_N = \frac{2\pi\varepsilon(1 - \nu_b^2)}{E_d}. \quad (D7)$$

The stiffness matrix of the dry fractured rock  $C^0$  is

$$C^0 = (S^0)^{-1}. \quad (D8)$$

Substituting equation (B8) into equation (B1) gives the expression for  $C_{22}^0$  as follows:

$$C_{22}^0 = L \left[ 1 - \frac{\pi L^2 \varepsilon}{2\mu(L - \mu)} \right]. \quad (D9)$$

To obtain the stiffness matrix of saturated fractured rocks, the anisotropic Gassmann equation (Guo et al., 2017) can be applied:

$$C_{ij}^{\text{sat}} = C_{ij}^0 + \alpha_i^0 \alpha_j^0 M_0, \quad (D10)$$

with

$$M_0 = \frac{K_g}{(1 - K_0^*/K_g) - \phi(1 - K_g/K_f)}, \quad K_0^* = \frac{1}{9} \sum_{i=1}^3 \sum_{j=1}^3 C_{ij}^0, \quad \alpha_m^0 = 1 - \frac{\sum_{n=1}^3 C_{mn}^0}{3K_g}, \quad (D11)$$

After some calculations, we can obtain the expression for  $C_{22}^{\text{sat}}$

$$C_{22}^{\text{sat}} = H \left[ 1 - \frac{\left( H^2 \varepsilon \pi + (-2\alpha - \alpha^2) M H \varepsilon \pi + \left( \alpha^2 + 2\alpha^3 - \frac{\alpha^4}{H} M \right) M^2 \varepsilon \pi \right)}{2\mu(H - \mu - \alpha M)} \right]. \quad (D12)$$

Because  $\alpha < 1$ , we have

$$|2\alpha| \gg |\alpha^2|, \quad (D13)$$

$$2\alpha^3 \gg \frac{\alpha^4 M}{H}, \quad (D14)$$

and

$$|\alpha^2| \gg |2\alpha^3|. \quad (D15)$$

Hence, the terms  $\frac{\alpha^4}{H} M^3 \varepsilon \pi$ ,  $\alpha^2 M H \varepsilon \pi$ , and  $2\alpha^3 M^2 \varepsilon \pi$  can be neglected, which result in the following approximation for  $C_{22}^{\text{sat}}$ :

$$C_{22}^{\text{sat}} \approx H \left[ 1 - \frac{\pi(H^2 + \alpha^2 M^2 - 2\alpha MH)\varepsilon}{2\mu(H - \mu - \alpha M)} \right], \quad (\text{D16})$$

namely,

$$C_{22}^{\text{sat}} = H \left[ 1 - \frac{\pi(H - \alpha M)^2 \varepsilon}{2\mu(H - \mu - \alpha M)} \right], \quad (\text{D17})$$

and

$$v_{\text{sat}} = \sqrt{\frac{C_{22}^{\text{sat}}}{\rho}} = v_1 \left[ 1 - \frac{\pi(H - \alpha M)^2 \varepsilon}{4\mu(H - \mu - \alpha M)} \right]. \quad (\text{D18})$$

### Acknowledgments

The authors would like to thank the sponsors Strategic Priority Research Program of the Chinese Academy of Sciences grant XDA14010303, the 111 project “Deep-Superdeep Oil & Gas Geophysical Exploration” (B18055), the Curtin Reservoir Geophysics Consortium (CRGC) Major State Research Development Program of China under grant 2016YFC0601101, and the China Scholarship Council (grant 201704910502) for the financial support. The attenuation and modulus dispersion data for this paper are available at <https://github.com/BoyeFu/attenuation-2D>.

### References

- Achenbach, J. (2012). *Wave propagation in elastic solids* (Vol. 16). Amsterdam: Elsevier.
- Ba, J., Carcione, J. M., & Nie, J. X. (2011). Biot-Rayleigh theory of wave propagation in double-porosity media. *Journal of Geophysical Research*, 116, B06202. <https://doi.org/10.1029/2010JB008185>
- Ba, J., Nie, J. X., Cao, H., & Yang, H. Z. (2008). Mesoscopic fluid flow simulation in double-porosity rocks. *Geophysical Research Letters*, 35(4), L04303.
- Barbosa, N., Rubino, J. G., Caspari, E., Guo, J., Gurevich, B., & Holliger, K. (2017). Hybrid modeling of 3D fractured media based on 2D numerical simulations: Aligned fractures case. *SEG Technical Program Expanded Abstracts 2017*, 4200–4204.
- Biot, M. A. (1941). General theory of three-dimensional consolidation. *Journal of Applied Physics*, 12(2), 155–164.
- Biot, M. A. (1956a). Theory of propagation of elastic waves in a fluid-saturated porous solid. I. Low-frequency range. *The Journal of the Acoustical Society of America*, 28(2), 168–178. <https://doi.org/10.1121/1.1908239>
- Biot, M. A. (1956b). Theory of propagation of elastic waves in a fluid-saturated porous solid. II. Higher frequency range. *The Journal of the Acoustical Society of America*, 28(2), 179–191. <https://doi.org/10.1121/1.1908241>
- Biot, M. A. (1962). Mechanics of deformation and acoustic propagation in porous media. *Journal of Applied Physics*, 33(4), 1482–1498. <https://doi.org/10.1063/1.1728759>
- Biot, M. A., & Willis, D. G. (1957). The elastic coefficients of the theory of consolidation. *Journal of Applied Mechanics*, 24, 594–601.
- Brown, R. J., & Korringa, J. (1975). On the dependence of the elastic properties of a porous rock on the compressibility of the pore fluid. *Geophysics*, 40(4), 608–616. <https://doi.org/10.1190/1.1440551>
- Bush, I. (2010). An integrated approach to fracture characterization. *Oil Review Middle East*, 2, 88–91.
- Chapman, M. (2003). Frequency-dependent anisotropy due to mesoscale fractures in the presence of equant porosity. *Geophysical Prospecting*, 51(5), 369–379. <https://doi.org/10.1046/j.1365-2478.2003.00384.x>
- Chapman, M., Liu, E., & Li, X. Y. (2006). The influence of fluid sensitive dispersion and attenuation on AVO analysis. *Geophysical Journal International*, 167(1), 89–105. <https://doi.org/10.1111/j.1365-246X.2006.02919.x>
- Galvin, R. (2007). Elastic wave attenuation, dispersion and anisotropy in fractured porous media, (Doctoral dissertation). Curtin University.
- Galvin, R. J., & Gurevich, B. (2006). Interaction of an elastic wave with a circular crack in a fluid-saturated porous medium. *Applied Physics Letters*, 88(6), 061918. <https://doi.org/10.1063/1.2165178>
- Galvin, R. J., & Gurevich, B. (2007). Scattering of a longitudinal wave by a circular crack in a fluid-saturated porous medium. *International Journal of Solids and Structures*, 44(22–23), 7389–7398. <https://doi.org/10.1016/j.ijsolstr.2007.04.011>
- Galvin, R. J., & Gurevich, B. (2009). Effective properties of a poroelastic medium containing a distribution of aligned cracks. *Journal of Geophysical Research*, 114, B07305. <https://doi.org/10.1029/2008JB006032>
- Gassmann, F. (1951). Über die elastizität poröser medien. *Vierteljahrsschrift der Naturforschenden Gesellschaft in Zurich*, 96, 1–23.
- Guo, J., Rubino, J., Barbosa, N. D., Glubokovskikh, S., & Gurevich, B. (2018a). Seismic dispersion and attenuation in saturated porous rocks with aligned fractures of finite thickness: Theory and numerical simulations—Part 1: P-wave perpendicular to the fracture plane. *Geophysics*, 83(1), WA49–WA62. <https://doi.org/10.1190/geo2017-0065.1>
- Guo, J., Rubino, J., Barbosa, N. D., Glubokovskikh, S., & Gurevich, B. (2018b). Seismic dispersion and attenuation in saturated porous rocks with aligned fractures of finite thickness: Theory and numerical simulations—Part 2: Frequency-dependent anisotropy. *Geophysics*, 83(1), WA63–WA71. <https://doi.org/10.1190/geo2017-0066.1>
- Guo, J., Rubino, J., Glubokovskikh, S., & Gurevich, B. (2017). Effects of fracture intersections on seismic dispersion: Theoretical predictions versus numerical simulations. *Geophysical Prospecting*, 65(5), 1264–1276. <https://doi.org/10.1111/1365-2478.12474>
- Guo, J., Rubino, J., Glubokovskikh, S., & Gurevich, B. (2018). Dynamic seismic signatures of saturated porous rocks containing two orthogonal sets of fractures: Theory versus numerical simulations. *Geophysical Journal International*, 213(2), 1244–1262. <https://doi.org/10.1093/gji/ggy040>
- Guo, M. Q., & Fu, L. Y. (2007). Stress associated coda attenuation from ultrasonic waveform measurements. *Geophysical Research Letters*, 34, L09307. <https://doi.org/10.1029/2007GL029582>
- Guo, M. Q., Fu, L. Y., & Ba, J. (2009). Comparison of stress-associated coda attenuation and intrinsic attenuation from ultrasonic measurements. *Geophysical Journal International*, 178(1), 447–456. <https://doi.org/10.1111/j.1365-246X.2009.04159.x>
- Gurevich, B. (2003). Elastic properties of saturated porous rocks with aligned fractures. *Journal of Applied Geophysics*, 54(3–4), 203–218. <https://doi.org/10.1016/j.jappgeo.2002.11.002>
- Gurevich, B., Brajanovski, M., Galvin, R. J., Müller, T. M., & Toms-Stewart, J. (2009). P-wave dispersion and attenuation in fractured and porous reservoirs—poroelasticity approach. *Geophysical Prospecting*, 57(2), 225–237. <https://doi.org/10.1111/j.1365-2478.2009.00785.x>
- Hefner, B. T., & Jackson, D. R. (2014). Attenuation of sound in sand sediments due to porosity fluctuations. *The Journal of the Acoustical Society of America*, 136(2), 583–595. <https://doi.org/10.1121/1.4889864>
- Hu, J., Fu, L. Y., Wei, W., & Zhang, Y. (2017). Stress-associated intrinsic and scattering attenuation from laboratory ultrasonic measurements on shales. *Pure and Applied Geophysics*, 1–34, 1198–1201.

- Hudson, J. A. (1980). September. Overall properties of a cracked solid. In *Mathematical Proceedings of the Cambridge Philosophical Society* (Vol. 88, No. 2, pp. 371–384). England: Cambridge University Press.
- Hudson, J. A. (1981). Wave speeds and attenuation of elastic waves in material containing cracks. *Geophysical Journal International*, 64(1), 133–150. <https://doi.org/10.1111/j.1365-246X.1981.tb02662.x>
- Hudson, J. A., Liu, E., & Crampin, S. (1996). The mechanical properties of materials with interconnected cracks and pores. *Geophysical Journal International*, 124(1), 105–112. <https://doi.org/10.1111/j.1365-246X.1996.tb06355.x>
- Hunziker, J., Favino, M., Caspari, E., Quintal, B., Rubino, J. G., Krause, R., & Holliger, K. (2018). Seismic attenuation and stiffness modulus dispersion in porous rocks containing stochastic fracture networks. *Journal of Geophysical Research: Solid Earth*, 123, 125–143. <https://doi.org/10.1002/2017JB014566>
- Jakobsen, M. (2004). The interacting inclusion model of wave-induced fluid flow. *Geophysical Journal International*, 158(3), 1168–1176. <https://doi.org/10.1111/j.1365-246X.2004.02360.x>
- Jakobsen, M., Johansen, T. A., & McCann, C. (2003). The acoustic signature of fluid flow in complex porous media. *Journal of Applied Geophysics*, 54(3–4), 219–246. <https://doi.org/10.1016/j.jappgeo.2002.11.004>
- Johnson, D. L. (2001). Theory of frequency dependent acoustics in patchy-saturated porous media. *The Journal of the Acoustical Society of America*, 110(2), 682–694. <https://doi.org/10.1121/1.1381021>
- Kachanov, M. (1992). Effective elastic properties of cracked solids: Critical review of some basic concepts. *Applied Mechanics Reviews*, 45(8), 304–335. <https://doi.org/10.1115/1.3119761>
- Kachanov, M., & Sevostianov, I. (2005). On quantitative characterization of microstructures and effective properties. *International Journal of Solids and Structures*, 42(2), 309–336.
- Kawahara, J. (1992). Scattering of P, SV waves by random distribution of aligned open cracks. *Journal of Physics of the Earth*, 40(3), 517–524.
- Kawahara, J., & Yamashita, T. (1992). Scattering of elastic waves by a fracture zone containing randomly distributed cracks. *Pure and Applied Geophysics*, 139(1), 121–144. <https://doi.org/10.1007/BF00876828>
- Liu, E., Chapman, M., Varela, I., Li, X., Queen, J. H., & Lynn, H. (2007). Velocity and attenuation anisotropy: Implication of seismic fracture characterizations. *The Leading Edge*, 26(9), 1170–1174. <https://doi.org/10.1190/1.2780788>
- Masson, Y. J., & Pride, S. R. (2007). Poroelastic finite difference modeling of seismic attenuation and dispersion due to mesoscopic-scale heterogeneity. *Journal of Geophysical Research*, 112, B03204. <https://doi.org/10.1029/2006JB004592>
- Maultzsch, S., Chapman, M., Liu, E., & Li, X. Y. (2003). Modelling frequency-dependent seismic anisotropy in fluid-saturated rock with aligned fractures: Implication of fracture size estimation from anisotropic measurements. *Geophysical Prospecting*, 51(5), 381–392. <https://doi.org/10.1046/j.1365-2478.2003.00386.x>
- Mavko, G., Mukerji, T., & Dvorkin, J. (2009). *The rock physics handbook: Tools for seismic analysis of porous media*. England: Cambridge University Press.
- Peacock, S., McCann, C., Sothcott, J., & Astin, T. R. (1994). Experimental measurements of seismic attenuation in microfractured sedimentary rock. *Geophysics*, 59(9), 1342–1351. <https://doi.org/10.1190/1.1443693>
- Phurkhao, P. (2013a). Compressional waves in fluid-saturated porous solid containing a penny-shaped crack. *International Journal of Solids and Structures*, 50(25–26), 4292–4304. <https://doi.org/10.1016/j.ijsolstr.2013.09.003>
- Phurkhao, P. (2013b). Wave diffraction by a line of finite crack in a saturated two-phase medium. *International Journal of Solids and Structures*, 50(7–8), 1044–1054. <https://doi.org/10.1016/j.ijsolstr.2012.11.027>
- Quintal, B., Jänicke, R., Rubino, J. G., Steeb, H., & Holliger, K. (2014). Sensitivity of S-wave attenuation to the connectivity of fractures in fluid-saturated rocks. *Geophysics*, 79(5), WB15–WB24. <https://doi.org/10.1190/geo2013-0409.1>
- Rubino, J., Caspari, E., Milani, M., Müller, T. M., & Holliger, K. (2015). Seismic anisotropy in fractured low-permeability formations: The effects of hydraulic connectivity. In 2015 SEG Annual Meeting, Society of Exploration Geophysicists.
- Rubino, J., Caspari, E., Müller, T. M., Milani, M., Barbosa, N. D., & Holliger, K. (2016). Numerical upscaling in 2-D heterogeneous poroelastic rocks: Anisotropic attenuation and dispersion of seismic waves. *Journal of Geophysical Research: Solid Earth*, 121, 6698–6721. <https://doi.org/10.1002/2016JB013165>
- Rubino, J., Müller, T. M., Guarracino, L., Milani, M., & Holliger, K. (2014). Seismoacoustic signatures of fracture connectivity. *Journal of Geophysical Research: Solid Earth*, 119, 2252–2271. <https://doi.org/10.1002/2013JB010567>
- Rubino, J., Ravazzoli, C. L., & Santos, J. E. (2009). Equivalent viscoelastic solids for heterogeneous fluid-saturated porous rocks. *Geophysics*, 74(1), N1–N13. <https://doi.org/10.1190/1.3008544>
- Schoenberg, M., & Sayers, C. M. (1995). Seismic anisotropy of fractured rock. *Geophysics*, 60(1), 204–211. <https://doi.org/10.1190/1.1443748>
- Song, Y., Hu, H., & Rudnicki, J. W. (2017a). Dynamic stress intensity factor (mode I) of a permeable penny-shaped crack in a fluid-saturated poroelastic solid. *International Journal of Solids and Structures*, 110, 127–136.
- Song, Y., Hu, H., & Rudnicki, J. W. (2017b). Normal compression wave scattering by a permeable crack in a fluid-saturated poroelastic solid. *Acta Mechanica Sinica*, 33(2), 356–367. <https://doi.org/10.1007/s10409-016-0633-8>
- Tisato, N., & Quintal, B. (2013). Measurements of seismic attenuation and transient fluid pressure in partially saturated Berea sandstone: Evidence of fluid flow on the mesoscopic scale. *Geophysical Journal International*, 195(1), 342–351. <https://doi.org/10.1093/gji/ggt259>
- Vlastos, S., Liu, E., Main, I. G., & Li, X. Y. (2003). Numerical simulation of wave propagation in media with discrete distributions of fractures: Effects of fracture sizes and spatial distributions. *Geophysical Journal International*, 152(3), 649–668. <https://doi.org/10.1046/j.1365-246X.2003.01876.x>
- Vlastos, S., Liu, E., Main, I. G., & Narteau, C. (2007). Numerical simulation of wave propagation in 2-D fractured media: scattering attenuation at different stages of the growth of a fracture population. *Geophysical Journal International*, 171(2), 865–880.
- Vlastos, S., Liu, E., Main, I. G., Schoenberg, M., Narteau, C., Li, X. Y., & Maillot, B. (2006). Dual simulations of fluid flow and seismic wave propagation in a fractured network: Effects of pore pressure on seismic signature. *Geophysical Journal International*, 166(2), 825–838. <https://doi.org/10.1111/j.1365-246X.2006.03060.x>
- Waterman, P. C., & Truell, R. (1961). Multiple scattering of waves. *Journal of Mathematical Physics*, 2(4), 512–537. <https://doi.org/10.1063/1.1703737>
- Wei, W., & Fu, L. Y. (2014). Monte Carlo simulation of stress-associated scattering attenuation from laboratory ultrasonic measurements. *Bulletin of the Seismological Society of America*, 104(2), 931–943. <https://doi.org/10.1785/0120130082>